



1    **A weather regime characterisation of winter biomass aerosol transport from southern Africa**

2

3    Marco Gaetani (1,2); Benjamin Pohl (3); Maria del Carmen Alvarez Castro (4,5); Cyrille Flamant (6);

4    Paola Formenti (1)

5

6    (1) Institut Pierre Simon Laplace, Laboratoire Interuniversitaire des Systèmes Atmosphériques, UMR

7    CNRS 7583, Université Paris-Est Créteil, Université de Paris, Institut Pierre Simon Laplace, Créteil,

8    France

9    (2) Scuola Universitaria Superiore IUSS, Pavia, Italia

10    (3) CRC/Biogéosciences, UMR6282 CNRS / Université de Bourgogne Franche-Comté, Dijon, France

11    (4) University Pablo de Olavide, Seville, Spain

12    (5) CMCC, Bologna, Italy

13    (6) Institut Pierre Simon Laplace, Laboratoire Atmosphères, Milieux, Observations Spatiales, UMR

14    CNRS 8190, Sorbonne Université, Université Versailles Saint Quentin, Paris, France

15

16    Contact: [marco.gaetani@iusspavia.it](mailto:marco.gaetani@iusspavia.it)



17 **Abstract**

18 During austral winter, a compact low cloud deck over South Atlantic contrasts with clear sky over  
19 southern Africa, where forest fires triggered by dry conditions emit large amount of biomass burning  
20 aerosols (BBA) in the free troposphere. Most of the BBA burden crosses South Atlantic embedded in  
21 the tropical easterly flow. However, midlatitude synoptic disturbances can deflect part of the aerosol  
22 from the main transport path towards southern extratropics.

23 In this study, a characterisation of the synoptic variability controlling the spatial distribution of BBA  
24 in southern Africa and South Atlantic during austral winter (August to October) is presented. By  
25 analysing atmospheric circulation data from reanalysis products, a 6-class weather regime (WR)  
26 classification of the region is constructed. The classification reveals that the synoptic variability is  
27 composed by four WRs representing disturbances travelling at midlatitudes, and two WRs  
28 accounting for pressure anomalies in the South Atlantic. The WR classification is then successfully  
29 used to characterise the aerosol spatial distribution in the region in the period 2003-2017, in both  
30 reanalysis products and station data. Results show that the BBA transport towards southern  
31 extratropics is controlled by weather regimes associated with midlatitude synoptic disturbances. In  
32 particular, depending on the relative position of the pressure anomalies along the midlatitude  
33 westerly flow, the BBA transport is deflected from the main tropical route towards southern Africa  
34 or the South Atlantic.

35 This paper presents the first objective classification of the winter synoptic circulation over South  
36 Atlantic and southern Africa. The classification shows skills in characterising the BBA transport,  
37 indicating the potential for using it as a diagnostic/predictive tool for aerosol dynamics, which is a  
38 key component for the full understanding and modelling of the complex radiation-aerosol-cloud  
39 interactions controlling the atmospheric radiative budget in the region.



40 **1. Introduction**

41 Natural and anthropogenic tropospheric aerosols are fundamental ingredients of the climate system.  
42 They influence the radiative properties of the atmosphere by deflecting and absorbing radiation  
43 (direct effect) and the cloud formation and properties by absorption (semi-direct effect) as well as by  
44 acting as cloud condensation nuclei (indirect effect). As a consequence, aerosols can influence on  
45 the atmospheric synoptic and large-scale dynamics (Bellouin et al., 2020).

46 Africa is the Earth's largest source of biomass burning aerosol (BBA; e.g. van der Werf et al., 2010,  
47 2017). The transport of BBA, originated from central Africa and embedded in the tropical mid-  
48 tropospheric easterly flow, occurs mostly above the Atlantic Ocean (Fig. 1a), a prominent feature  
49 during austral winter (June to October; Fig. 1b) between the Equator and 20°S, when dry conditions  
50 in central Africa favour the development of forest fires (Horowitz et al., 2017). However,  
51 extratropical rivers of smoke are also observed to extend to 30-40°S between August and October  
52 (Fig. 1b). The definition 'river of smoke' refers to the sharply defined boundaries of the smoke  
53 plume, which can be several hundred kilometres wide and flow over a few thousands kilometres  
54 above southern Africa towards Southern and Indian Oceans (McMillan et al., 2003; Swap et al.,  
55 2003). Depending on the transport path (e.g. either above the continent or recirculated above the  
56 ocean), physical and chemical properties of the BBA may change (Abel et al., 2003; Eck et al., 2003;  
57 Formenti et al., 2003; Haywood et al., 2003; Pistone et al., 2019; Wu et al., 2020). The  
58 characterisation of BBA transport in terms of synoptic atmospheric circulation is therefore one of the  
59 key elements to shed light the already complex picture of the radiation-aerosol-cloud interactions  
60 (Adebisi and Zuidema, 2018; Formenti et al., 2019; Haywood et al., 2003, 2021; Lindesay et al., 1996;  
61 Mallet et al., 2020; Redemann et al., 2021; Swap et al., 2003; Zuidema et al., 2016). Additionally, the  
62 extent and direction of BBA transport may condition the atmospheric remote supply of nutrients and  
63 pollutants to South Atlantic, the Southern ocean, and the Indian Ocean, as well as to the Antarctica  
64 (Baker et al., 2010; Barkley et al., 2019; Gao et al., 2003, 2020; Swap et al., 1996; Wai et al., 2014).

65 Understanding the role of the radiation-aerosol-cloud interaction in controlling the atmospheric  
66 radiative budget and, consequently, climate dynamics is a key aspect for the improvement of climate  
67 modelling. Indeed, even state-of-the art climate models still struggle in reliably representing the  
68 atmospheric radiative forcing, due to inaccurate parametrizations of the radiation-aerosol-cloud  
69 interaction (Mallet et al., 2020; Stier et al., 2013; Tang et al., 2019). This is particularly relevant in the  
70 South Atlantic, where the incomplete knowledge of the smoke-cloud regime generates large  
71 discrepancies in the modelling of radiative forcing and sea surface temperature (SST) in the region,  
72 eventually affecting climate simulations at regional and global scale (Zuidema et al., 2016). While a  
73 conceptual understanding of the meteorological conditions determining the transport of aerosols



74 and pollutants at the subcontinental scale exists (Diab et al., 1996; Garstang et al., 1996; Tyson,  
75 1997), the large-scale drivers of the aerosol spatial distribution in the region are still not understood  
76 and an objective synoptic characterisation of the wintertime BBA transport is still missing to date. In  
77 particular, an objective synoptic characterisation of the wintertime BBA transport in the region is still  
78 missing to date. Indeed, synoptic circulation in the southern Africa/South Atlantic sector is discussed  
79 in literature mainly in relationship with convection and precipitation during austral summer (e.g.  
80 Crétat et al., 2019; Dieppois et al., 2016; Fauchereau et al., 2009; Macron et al., 2014; Pohl et al.,  
81 2018; Vigaud et al., 2012).

82 In this paper, an objective weather regime (WR) classification of the winter atmospheric circulation  
83 in the southern Africa/South Atlantic sector is presented for the first time, and used to characterise  
84 the BBA transport in the region. In particular, the study focuses on the characterisation of the  
85 southward deflection of BBA from the mean tropical easterly flow from August to October (ASO) in  
86 the period 2003-2017. Atmospheric circulation data from a reanalysis product are first used to  
87 classify the synoptic circulation patterns. Then, the classification is used to characterise the BBA  
88 transport anomalies in reanalysis data and in situ observations in the region.

89 The paper is organised as follows: in Section 2, data and methods used in the analysis are presented;  
90 in Section 3, the WR classification is presented and the synoptic characterisation of BBA anomalies is  
91 discussed; conclusions and perspectives are summarised in Section 4.

## 92 **2. Data and Methods**

### 93 **2.1. Reanalysis and observations**

94 The atmospheric circulation and the spatial distribution and optical properties of the BBA over  
95 southern Africa and the South Atlantic in ASO 2003-2017 are analysed using data from the  
96 Copernicus Atmospheric Monitoring Service reanalysis product (CAMS; Flemming et al., 2017) at 6h  
97 time steps and 0.75° horizontal resolution. Daily values are obtained at each grid point as the  
98 average of 6h time steps, and daily anomalies are computed by removing the low frequency  
99 component of the time series, estimated by computing monthly means from daily data and  
100 interpolating them to daily time steps using a cubic spline interpolation. The limited coverage of the  
101 CAMS reanalysis (15 years) does not allow a robust definition of the climatological seasonal cycle,  
102 which would be too dependent on the interannual variability. Therefore, in order to isolate the  
103 synoptic variability alone, the definition of a low frequency component, accounting for the seasonal  
104 cycle and the interannual variability, is preferred. The BBA emission is estimated by the organic  
105 matter mixing ratio at 10m, the BBA transport is estimated as the product of organic matter mixing



ratio and wind at 700 hPa, and the aerosol spatial distribution is represented by the AOD at 550 nm (Fig. 2a).

Global reconstructions of the observed sea surface temperature (SST) are used to investigate the teleconnections controlling the synoptic variability. Data are extracted from the Met Office Hadley Centre HadISST dataset (Rayner et al., 2003), available from 1871 at monthly time scale and 1° horizontal resolution, and from the NOAA Extended Reconstructed Sea Surface Temperature (ERSST) Version 5 dataset (Huang et al., 2017), available from 1854 at monthly time scale and 2° horizontal resolution.

Observed daily values of the aerosol optical depth (AOD) at 500 nm from AERONET stations (<https://aeronet.gsfc.nasa.gov/>) are used to validate the synoptic characterisation performed on CAMS data. Stations are selected among the ones with at least 2 years of level 2 data obtained from the Version 3 Direct Sun algorithm (Giles et al., 2018). Stations are selected outside the source region in Tropical Africa, namely south of 20°S and west of 10°E (Fig. 2a, Table 1), in order to focus on BBA transport only, not being influenced by the BBA emission which is assumed not to be directly related to synoptic conditions. Among the available stations, St. Helena (15.9°S, 5.7°W) and Wits University (26.2°S, 28.0°E) are not included because of the limited coverage (less than 100 observations during the study period). Moreover, the stations closer to the greater Johannesburg and Pretoria urban areas (namely, Durban UKZN (29.8°S, 30.9°E), Pretoria CSIR-DPSS (25.8°S, 28.3°E) and Skukuza (25.0°S, 31.2°E)) are not included, because too affected by the proximity with urban sources (Fig. 2a). For each station, daily AOD anomalies are computed by removing the seasonal cycle at the station. However, the sparseness of the AERONET observations makes difficult the definition of a daily seasonal cycle. Therefore, CAMS AOD at 550 nm is selected in an area defined by the grid point the closest to the station coordinates and the adjacent grid points, and averaged to estimate the daily seasonal cycle of the AOD at 500 nm. Empirical evidence shows that a quadratic relationship exists between the natural logarithm of AOD and wavelength (Eck et al., 1999). However, at such close wavelengths the relationship can be assumed as linear, and the relationship between the natural logarithm of AOD at 500 and 550 nm can be modelled as follows:

$$\log AOD_{500nm} = a \log AOD_{550nm} + b.$$

At each AERONET station, the logarithm of observed and CAMS AOD well correlates during ASO 2003-2017 (correlations coefficients lie between 0.71 and 0.90, all significant at 99% level of confidence, see Fig. 3). Therefore, the daily seasonal cycle of the observed AOD is estimated by means of a linear regression onto the CAMS seasonal cycle. In order to minimise the effect of possible large discrepancies between AERONET and CAMS data, the difference between AERONET



139 and CAMS AOD is computed and the values in the lowest and highest 5% are discarded before to  
 140 perform the linear regression (the coefficients used in the regression model at each station are  
 141 displayed in Fig. 3).

## 142 2.2. Weather regime classification

143 The WR classification is performed on the geopotential height at 700 hPa, which is the level where  
 144 BBA transport is maximal, in the domain [20°W-40°E, Eq-40°S] (see Fig. 2bc). The selection of the  
 145 domain is made to include the main BBA transport routes in the tropical belt and towards the  
 146 extratropics. However, during the dry season the synoptic variability in the tropics is reduced in  
 147 comparison with the extratropics (Baldwin, 2001). Therefore, the southern border of the domain is  
 148 set to 40°S to not let the dominant midlatitude modes to mask variability in the tropical belt. The  
 149 atmospheric circulation is first characterised by isolating the main modes of variability represented  
 150 by the empirical orthogonal functions (EOFs) of the geopotential height derived by a principal  
 151 component analysis (PCA). Each mode is represented by a spatial anomaly pattern and a  
 152 standardized time series (namely, the principal components, PCs) accounting for the amplitude of  
 153 the anomaly pattern (for more details on PCA, see Storch and Zwiers, 1999). The first 4 EOFs,  
 154 accounting for 80% of total variability (Fig. S1), are used to classify the WRs by means of a k-means  
 155 algorithm, using  $k = [2, 10]$  (Michelangeli et al., 1995). For each  $k$ , the classification is performed 100  
 156 times, to ensure reproducibility of the results. A red-noise test is performed to assess the  
 157 significance of the class partition (Michelangeli et al., 1995), resulting in 6 and 7 classes (Fig. S3). In  
 158 this study, the 6 class partition is used. The synoptic characterisation is also performed by using the  
 159 7 class partition, and is illustrated in Section S2.

## 160 2.3. Synoptic characterisation

161 The WR classification is used to characterise the observed AOD data from the AERONET stations in  
 162 the region (Table 1). Two approaches are used:

163 1) Daily AOD anomalies are linked to the corresponding WR and grouped, and statistical differences  
 164 among groups are investigated (circulation-to-environment approach, C2E). The significance of the  
 165 C2E characterisation is assessed by a one-way analysis of variance (ANOVA) with the null hypothesis  
 166 that the distributions associated with each WR are derived from populations with the same mean.  
 167 Furthermore, for each WR the significance of the associated AOD anomalies with the respect of the  
 168 full sample is assessed by a non-parametric Kolmogorov-Smirnov (KS) test.

169 2) Daily AOD anomalies are divided into quartiles, and the changes in the WR occurrences within  
 170 each quartile are studied (environment-to-circulation approach, E2C). The significance of the E2C  
 171 characterisation is assessed by computing the Chi-squared statistics for each quartile, with the null



hypothesis that the associated WR frequencies are derived from the same distribution of the full sample. The Chi-squared statistics is tested against the critical value for 5 degrees of freedom and at the 95% level of confidence. The degrees of freedom are estimated as the number of the observation categories (6 WRs) minus the parameters of the distribution to be fitted (the mean WR occurrence, i.e. 1).

### 3. Results

#### 3.1. Synoptic characterisation of the regional atmospheric variability

The mean atmospheric conditions over South Atlantic and southern Africa in ASO are illustrated in Fig. 2a. The atmospheric circulation at 700 hPa is characterised by a continental high centred at 25°S over southern Africa and extending over eastern South Atlantic, and a subtropical trough west of South Africa deflecting southward the midlatitude westerly flow. Massive quantities of BBA are emitted from tropical southern Africa, and are driven westward over South Atlantic by the easterly trade winds, while the anticyclonic gyre associated with the continental high recirculates the BBA towards South Africa along the Namibian coast. This recirculation merges with smaller BBA amounts emitted from sources located in South Africa in the urban area of Johannesburg and Pretoria, to be eventually transported eastward to the Indian Ocean embedded in the westerly flow.

The WR classification shows two synoptic patterns (WR2 and 6) accounting for the oscillation of the pressure field in the South Atlantic and four synoptic patterns (WR1, 3, 4 and 5) accounting for midlatitude pressure anomalies (Fig. 4). These four WRs represent the fingerprint of propagative disturbances travelling along the midlatitude mean westerly flow with wave number 8-12, as demonstrated by the EOF analysis (see Section S1). The synoptic variability is dominated by the WR2, which occurs at a frequency of 22.3% and is characterised by a high pressure anomaly in the South Atlantic accompanied by a reinforcement of the midlatitude westerlies (Fig. 4a). Its symmetric counterpart is represented by WR6, which occurs at a frequency of 17.7% and is characterised by a low pressure anomaly and a weaker westerly flow in the midlatitudes (Fig. 4f). WR2 occurs mainly in September-October, while WR6 does not show a clear seasonality (Fig. 5). The analysis of the transitions from a WR into the others reveals that WR2 and 6 are dominated by persistence (Table 2). The remaining 60% of the synoptic variability in the region is characterised by eastward travelling disturbances of the westerly flow, represented by WR1, 3, 4 and 5 (Fig. 4). WR1 and 3 occur more frequently in August-September, while WR4 and 5 are more frequent in October (Fig. 5). In this case, the analysis of the transition rates shows similar persistence ratios (from 0.39 to 0.46) and high rates for preferred transitions (WR1 into 5, WR3 into 4, WR4 into 1, WR5 into 3, see Table 2), pointing out the propagative character of these WRs.



At the global scale, the variability of the atmospheric circulation south of 20°S is dominated by the southern annular mode (SAM), which consists of out-of-phase surface pressure and geopotential height anomalies between the Antarctic region and the southern midlatitudes, resulting in the modulation of the location and intensity of the westerly wind belt (Baldwin, 2001; Limpasuvan and Hartmann, 1999). Pohl and Fauchereau (2012) characterised the synoptic variability of the SAM in terms of WR, identifying 4 main variability modes in the southern midlatitudes, three of them associated with circulation patterns characterised by stationary wave-number 4. The persistent character of WR2 and 6 indicate a possible connection with the synoptic variability of the SAM. The relationship between the WR occurrence and the SAM daily index is investigated using both the C2E and the E2C approach. WR6 shows a statistically significant association with positive SAM phases (not shown), coherently with expected weaker westerlies at midlatitudes (see Fig. 4f). However, the WR2-SAM relationship results statistically weaker, and no relationship at all is found with WR1, 3, 4 and 5 (not shown).

The WRs describing propagative disturbances at midlatitudes (WR1, 3, 4 and 5) are characterised by the longitudinal displacement of high-low pressure anomalies modulating the meridional circulation, which in turn drives the poleward BBA transport above the South Atlantic and southern Africa. In particular, WR3 favours the recirculation of BBA from the ocean towards Namibia and South Africa, leading to significant positive AOD anomalies above all the continental stations (Fig. 4c), while WR5 pushes the BBA recirculation above the South Atlantic and inhibits the BBA transport towards the Indian Ocean (Fig. 4e). Conversely, WR1 and 4 are associated with a weaker BBA transport above Namibia and South Africa, leading to significant negative anomalies above the continental stations, and larger transport towards the Indian Ocean (Fig. 4ad). BBA transport along the Atlantic coast of Namibia and South Africa is also anomalously high during WR6, which is characterised by a low pressure anomaly in the South Atlantic inhibiting the transport towards subtropical South Atlantic, and leading to significant negative anomalies above Ascension Island, and favouring a poleward route driving anomalous BBA concentrations above the continental stations (Fig. 4f). WR2, characterised by a high pressure anomaly in the South Atlantic strengthening the easterly flow in the Tropics, is the only WR associated with a reinforcement of the main BBA transport route in the tropical South Atlantic, and positive AOD anomalies only affect the Ascension Island station (Fig. 4b).

### 3.2. Synoptic characterisation of aerosol optical depth in-situ observations

The robustness of the synoptic characterisation of the BBA transport obtained from the CAMS data is assessed by linking the WR classification to the observed AOD from AERONET stations in the region (Table 1).





238 The C2E characterisation of the AOD observations is presented in Fig. 6; the associated statistical  
 239 analysis is summarised in Table 3. AOD anomalies above Ascension Island during WR1-5 are evenly  
 240 distributed between positive and negative values, while AOD anomalies during WR6 show a  
 241 preference for negative values (Fig. 6a). The significance of this characterisation is confirmed by the  
 242 ANOVA with a level of confidence higher than 99%. Just south of the source region in Bonanza,  
 243 significant positive anomalies are observed during WR4 (Fig. 6b). However, the statistical significance  
 244 of this characterisation only reaches 93%. AOD variability at central Namibia stations (Gobabeb,  
 245 Henties Bay and HESS) is dominated by WR1, leading to significant negative anomalies (Fig. 6c-e). In  
 246 Gobabeb and HESS, significant positive anomalies are observed during WR6 (Fig. 6c) and WR3 (Fig.  
 247 6e), respectively. Negative anomalies are also observed in Gobabeb and Henties Bay in association  
 248 with WR4, however these anomalies are poorly significant (Fig. 6c,d). The ANOVA supports this  
 249 characterisation, indicating that the null hypothesis can be rejected with a level of confidence higher  
 250 than 99%. Similarly, the continental station in Upington shows significant negative anomalies during  
 251 WR1 and 4, and significant positive anomalies during WR3 (Fig. 6g), and the ANOVA indicates the  
 252 rejection of the null hypothesis with 99% level of confidence. In South Africa, the southernmost  
 253 station in Simon's Town does not show significant anomalies in association with any WR, and the  
 254 ANOVA confirms that the WR classification is not able to characterise the AOD variability ( $p=0.09$ ).  
 255 The C2E characterisation performed using observed AOD data confirms the relationship between the  
 256 WRs associated with midlatitude disturbances (WR1, 3 and 4) and the BBA transport above the  
 257 AERONET continental stations, and between WR6 and the BBA transport above Ascension Island, as  
 258 shown by the CAMS data (cf. Fig. 4). The comparison with the synoptic characterisation performed  
 259 using a WR classification with 7 clusters highlights that the latter is less robust, showing poorer  
 260 ANOVA performances. Moreover, the additional WR, accounting for a strengthening of the  
 261 continental high, does not provide further characterisation of the AOD anomalies (see Section S2 for  
 262 details).

263 The E2C characterisation of the BB AOD station data is presented in Fig. 7; the associated statistical  
 264 analysis is summarised in Table 4. AOD anomalies are divided in quartiles, with quartiles from 1st to  
 265 4th representing anomalies from the largest negative to the largest positive, and the relative change  
 266 in WR occurrence is displayed for each quartile. In Ascension Island, the 3rd quartile is characterised  
 267 by a significant change in the WR frequency the distribution, with increased occurrence of WR4 (Fig.  
 268 6a). The Bonanza station does not show any significant change in the WR occurrence (Fig. 6b). In  
 269 central Namibia stations (Gobabeb, Henties Bay and HESS; Fig. 6c-e), positive AOD anomalies are  
 270 associated with significantly more frequent WR6. In HESS, positive anomalies are also associated  
 271 with significant changes in the occurrence of WR2-4. Significant changes in the WR distribution are



272 observed for the 1st quartile in Gobabeb (increased occurrence of WR1, 4 and 5) and HESS (more  
 273 frequent WR1 and 6). Similarly, the South African stations in Upington and Simon's Town show  
 274 positive AOD anomalies associated with more frequent WR3, 5 and 6, and negative anomalies  
 275 associated with more frequent WR1, 4 and 6 (Fig. 6f,g). The E2C characterisation confirms the  
 276 importance of the midlatitude disturbances (WR1, 3 and 4) in controlling the AOD anomalies at the  
 277 AERONET continental stations, in particular by driving the largest anomalies (1st and 4th quartiles).  
 278 However, this approach shows some inconsistencies: WR4, which is characterised by a southerly  
 279 anomaly in the BBA transport along the Atlantic coast (Fig. 4d), is associated with positive AOD  
 280 anomalies in HESS instead; similarly WR6, characterised by a northerly BBA transport anomaly along  
 281 the coast (Fig. 4f), is associated with both positive and negative anomalies in HESS and Upington.  
 282 The origin of this ambiguities is likely due to the location of these stations at the margin of the BBA  
 283 transport path associated with the WR circulation patterns, making them highly sensitive to the  
 284 variability of the circulation around the centroid. The comparison with the synoptic characterisation  
 285 performed using a 7 cluster WR classification highlights the same ambiguities when the AOD  
 286 anomalies in the continental stations are associated with the WR describing a low pressure anomaly  
 287 in the South Atlantic (see Section S2 for details).

### 288 3.3. Interannual variability

289 The WR frequency in ASO is also analysed at the interannual time scale. All WRs show similar  
 290 interannual variability in the frequency of occurrence (2-4% standard deviation), with the exception  
 291 of WR2 showing the larger interannual variability (6% standard deviation) (Fig. 8). No trend is found  
 292 in the WR occurrence (a Mann-Kendall test is performed at 95% level of confidence), not surprisingly  
 293 due to the short time coverage of the reanalysis. Possible teleconnections controlling the WR  
 294 interannual variability are analysed by computing the linear correlation between the WR frequency  
 295 and the SST variability at the global scale (Fig. 9). WR1, 3, 4 and 5 do not show significant correlation  
 296 patterns at the global scale, with the exception of localised SST anomalies in the South Atlantic  
 297 (WR1, 4 and 5) and Warm Pool (WR1). Conversely, WR2 and 6 show a strong relationship with El  
 298 Niño/Southern Oscillation (ENSO)-like patterns. In particular, WR2 occurrence is associated with La  
 299 Niña conditions, while WR6 is associated with El Niño conditions. The linkage with La Niña conditions  
 300 can also explain the larger interannual variability of WR2 during the analysed period, mainly due to  
 301 the peak in 2010 associated with a strong La Niña event (Boening et al., 2012), and the minimum in  
 302 2015, associated with an extreme El Niño event (Hu and Fedorov, 2017). The analysis of the WR-SST  
 303 correlations performed by using NOAA ERSST data show similar teleconnection patterns (see Section  
 304 S3). Differently from the WRs associated with travelling disturbances, WR2 and 6 represent a sort of  
 305 stationary South Atlantic oscillatory pattern, which might interact at the synoptic time scale with



Rossby-wave patterns from the equatorial Pacific during ENSO active phases (e.g. Hoskins and Ambrizzi, 1993). The teleconnection mechanisms are explored by computing the correlation between the WR occurrence and the global geopotential at 200 hPa (Fig. 10), the level where teleconnection signals are the strongest. Wave patterns connecting the Pacific to South Atlantic are found for both the WR2 and 6, though significance for WR6 is weak. A similar modulation by the ENSO of synoptic regimes in the Southern Hemisphere is also reported during austral summer by Fauchereau et al. (2009) and Pohl et al. (2018). The correlation between the occurrence of WR1, 3, 4 and 6 and the global geopotential does not show organised patterns at mid-to-high latitudes (Fig. 10). The comparison with the 7 cluster WR classification shows similar results, however the teleconnection patterns are less evident (see Section S2).

The impact of the WR interannual variability on the BBA transport is assessed by computing the linear correlation with the CAMS organic matter mixing ratio and the BBA transport at 700 hPa (Fig. 10). The WR interannual variability affects the mid-tropospheric circulation in the subtropics, modulating the BBA transport on both the zonal and the meridional direction. However, the correlation analysis reveals that the WR variability has weak impact on the BBA transport at the interannual time scale, only controlling limited areas in the Tropical Atlantic (WR1), South Atlantic (WR2) and southern Africa (WR4). However, the short time coverage and sparseness of the AERONET observations does not allow validation of the impact of the WR characterisation on the interannual time scale. The comparison with the 7 cluster WR classification does not show major differences (see Section S2). In particular, the additional WR, accounting for a strengthening of the continental high, shows no significant impact on the BBA transport (see Fig. S11a).

#### 4. Conclusions

In this paper, the first objective classification of the synoptic circulation over South Atlantic and southern Africa during the dry season is presented. By using atmospheric circulation data from a reanalysis product, a robust classification with 6 WRs is defined for August-to-October in the period 2003-2017. Four WRs (WR1, 3, 4 and 5) represent the fingerprint of midlatitude propagative disturbances, while two WRs (WR2 and 6) are characterised by persistence and represent the oscillation of the pressure field in the South Atlantic. In particular, WR2 is associated with a reinforced South Atlantic anticyclone, and is the dominant WR during the dry season. The stationarity of the WR2/6 system suggests a connection with the synoptic variability of the SAM, which is also consistent with the South Atlantic Oscillation pattern firstly identified by Chen (2014). At the interannual time scale, the occurrence of persistent WR2 and 6 also shows a strong connection with the El Niño/Southern Oscillation through a tropical-extratropical Rossby wave pattern.



340 The synoptic classification is used to characterise the transport of BBA from equatorial Africa, which  
341 dominates the aerosol atmospheric content in the region during the dry season. By analysing  
342 reanalysis data, it is found that WR2 and 6 modulate the easterly transport from tropical Africa  
343 sources, which is the main climatological transport route. The synoptic characterisation also shows  
344 that midlatitude propagative disturbances modulate the BBA transport from equatorial Africa,  
345 elucidating the mechanism responsible for the BBA transport to the extratropics, which is peculiar in  
346 this period of the year. Specifically, WR3 drives enhanced transport above the continent, while WR1  
347 inhibits the transport; WR5 drives the BBA recirculation over the ocean, which is inhibited by WR4.  
348 The BBA transport characterisation is also tested by using AOD observations from AERONET stations,  
349 which show a good degree of consistency with the results based on reanalysis data. However,  
350 limited data availability in most of the stations prevents a robust statistical validation of the synoptic  
351 characterisation of observations at the regional scale. Results show that the occurrence of WR1 and  
352 4 inhibits the BBA transport towards the continental stations (Gobabeb, Henties Bay, HESS and  
353 Upington), while WR3 favours the transport above the same locations. Along the Atlantic route, the  
354 occurrence of WR6 limits the BBA transport towards Ascension Island. In-situ observations in  
355 Bonanza and Simon's Town are not well characterised by the WR classification. The former likely  
356 because of its proximity to the source region, where emission is not strongly affected by the synoptic  
357 atmospheric circulation, the latter possibly because of the poor data coverage. WR then clustering  
358 shows to be a valuable tool in discriminating aerosol transport and concentrations over South  
359 Atlantic and southern Africa at the short timescales (day-to-day and synoptic variability). However,  
360 the characterisation of the AOD variability at the interannual time scale shows limited performance,  
361 probably due to the shortness of the time period considered in the analysis. Indeed, within a 15 year  
362 time range, a large fraction of the variance is associated with daily weather patterns instead of  
363 changes from one season to another. This gap can be filled by analysing longer coverage reanalysis  
364 products.

365 A 7-class WR classification is also tested for the characterisation of the synoptic variability of the BBA  
366 transport. However, this classification does not improve the performance of the 6 cluster WR  
367 classification, showing overall poorer statistics and not correcting some ambiguities found in the E2C  
368 characterisation of the continental AERONET stations.

369 This paper provides new insights in the understanding of the synoptic circulation in South Atlantic  
370 and southern Africa, by characterising for the first time the dry season circulation and the associated  
371 rivers of smoke. The characterisation of the transport routes in the region is crucial to support the  
372 characterisation of the physical and chemical properties of the BBA, and model the associated  
373 impact on clouds and radiation. The WR characterisation is also a valuable resource to develop



374 predictive tools for the BBA spatial distribution in the region. In particular, by using reliable long  
375 coverage reanalysis products a classification for past decades can be built, and the BBA spatial  
376 distribution can be reconstructed where observations are not available. Furthermore, the WR  
377 characterisation can be used in climate model projections to estimate the future evolution of the  
378 rivers of smoke in the region.



379 *Data availability.* CAMS data are freely available at the Copernicus Atmospheric Data Store  
380 (<https://ads.atmosphere.copernicus.eu/>). AERONET station data are made freely available by the  
381 NASA Goddard Space Flight Center (<https://aeronet.gsfc.nasa.gov/>). The SAM daily index is made  
382 freely available by the NOAA Climate Prediction Center (<https://www.cpc.ncep.noaa.gov/>).  
383 *Supplement.* The supplement related to this article is available online at XXXXXXXXXXXX.  
384 *Author contributions.* MG conceived the study, designed and performed the analysis and wrote the  
385 paper. BP and MCAC performed the WR classification. All the authors contributed to the discussion  
386 and interpretation the results and the writing of the text. PF and CF designed the original AEROCLO-  
387 sA observational concept, and co-led the 5-year investigation.  
388 *Competing interests.* PF is guest editor for the ACP Special Issue “New observations and related  
389 modelling studies of the aerosol–cloud–climate system in the Southeast Atlantic and southern Africa  
390 regions”. The remaining authors declare that they have no conflicts of interests.  
391 *Special issue statement.* This article is part of the special issue “New observations and related  
392 modelling studies of the aerosol–cloud–climate system in the Southeast Atlantic and southern Africa  
393 regions (ACP/AMT inter-journal SI)”. It is not associated with a conference.  
394 *Acknowledgments.* The authors thank the AERONET PIs (Brent Holben, Nichola Knox, Stuart Piketh,  
395 Gillian Maggs-Kollin, Derek Griffith, and Willie Gunter) and their staff for establishing and  
396 maintaining the AERONET sites used in this study, and K. Schepanski and F. Waquet for useful  
397 discussion.  
398 *Financial support.* The AEROCLO-sA project was supported by the French National Research Agency  
399 under grant agreement n° ANR-15-CE01-0014-01, the French national program LEFE/INSU, the  
400 Programme national de Télédétection Spatiale (PNTS, <http://www.insu.cnrs.fr/pnts>), grant n° PNTS-  
401 2016-14, the French National Agency for Space Studies (CNES), and the South African National  
402 Research Foundation (NRF) under grant UID 105958. The research leading to these results has  
403 received funding from the European Union’s 7th Framework Programme (FP7/2014-2018) under  
404 EUFAR2 contract n°312609”.



## 405 References

- 406 Abel, S. J., Haywood, J. M., Highwood, E. J., Li, J. and Buseck, P. R.: Evolution of biomass burning  
 407 aerosol properties from an agricultural fire in southern Africa, *Geophys. Res. Lett.*, 30(15),  
 408 doi:https://doi.org/10.1029/2003GL017342, 2003.
- 409 Adebisi, A. A. and Zuidema, P.: Low Cloud Cover Sensitivity to Biomass-Burning Aerosols and  
 410 Meteorology over the Southeast Atlantic, *J. Clim.*, 31(11), 4329–4346, doi:10.1175/JCLI-D-17-0406.1,  
 411 2018.
- 412 Baker, A. R., Lesworth, T., Adams, C., Jickells, T. D. and Ganzeveld, L.: Estimation of atmospheric  
 413 nutrient inputs to the Atlantic Ocean from 50°N to 50°S based on large-scale field sampling: Fixed  
 414 nitrogen and dry deposition of phosphorus, *Global Biogeochem. Cycles*, 24(3),  
 415 doi:https://doi.org/10.1029/2009GB003634, 2010.
- 416 Baldwin, M. P.: Annular modes in global daily surface pressure, *Geophys. Res. Lett.*, 28(21), 4115–  
 417 4118, doi:10.1029/2001GL013564, 2001.
- 418 Barkley, A. E., Prospero, J. M., Mahowald, N., Hamilton, D. S., Popendorf, K. J., Oehlert, A. M.,  
 419 Pourmand, A., Gatineau, A., Panechou-Pulcherie, K., Blackwelder, P. and Gaston, C. J.: African  
 420 biomass burning is a substantial source of phosphorus deposition to the Amazon, Tropical Atlantic  
 421 Ocean, and Southern Ocean, *Proc. Natl. Acad. Sci. U. S. A.*, 116(33), 16216–16221,  
 422 doi:10.1073/pnas.1906091116, 2019.
- 423 Bellouin, N., Quaas, J., Gryspeerdt, E., Kinne, S., Stier, P., Watson-Parris, D., Boucher, O., Carslaw, K.  
 424 S., Christensen, M., Daniau, A. -L., Dufresne, J. -L., Feingold, G., Fiedler, S., Forster, P., Gettelman, A.,  
 425 Haywood, J. M., Lohmann, U., Malavelle, F., Mauritsen, T., McCoy, D. T., Myhre, G., Mülmenstädt, J.,  
 426 Neubauer, D., Possner, A., Rugenstein, M., Sato, Y., Schulz, M., Schwartz, S. E., Sourdeval, O.,  
 427 Storelvmo, T., Toll, V., Winker, D. and Stevens, B.: Bounding Global Aerosol Radiative Forcing of  
 428 Climate Change, *Rev. Geophys.*, 58(1), 1–45, doi:10.1029/2019RG000660, 2020.
- 429 Boening, C., Willis, J. K., Landerer, F. W., Nerem, R. S. and Fasullo, J.: The 2011 La Niña: So strong, the  
 430 oceans fell, *Geophys. Res. Lett.*, 39(19), n/a-n/a, doi:10.1029/2012GL053055, 2012.
- 431 Chen, G.: Revisit to atmospheric oscillations over global oceans: a combined climatology/modality  
 432 approach, *Int. J. Climatol.*, 34(8), 2715–2729, doi:https://doi.org/10.1002/joc.3870, 2014.
- 433 Crétat, J., Pohl, B., Dieppois, B., Berthou, S. and Pergaud, J.: The Angola Low: relationship with  
 434 southern African rainfall and ENSO, *Clim. Dyn.*, 52(3–4), 1783–1803, doi:10.1007/s00382-018-4222-  
 435 3, 2019.
- 436 Diab, R. D., Jury, M. R., Combrink, J. and Sokolic, F.: A comparison of anticyclone and trough



- 437 influences on the vertical distribution of ozone and meteorological conditions during SAFARI-92, J.  
 438 Geophys. Res. Atmos., 101(D19), 23809–23821, doi:https://doi.org/10.1029/95JD01844, 1996.
- 439 Dieppois, B., Pohl, B., Rouault, M., New, M., Lawler, D. and Keenlyside, N.: Interannual to  
 440 interdecadal variability of winter and summer southern African rainfall, and their teleconnections, J.  
 441 Geophys. Res. Atmos., 121(11), 6215–6239, doi:10.1002/2015JD024576, 2016.
- 442 Eck, T. F., Holben, B. N., Reid, J. S., Dubovik, O., Smirnov, A., O'Neill, N. T., Slutsker, I. and Kinne, S.:  
 443 Wavelength dependence of the optical depth of biomass burning, urban, and desert dust aerosols, J.  
 444 Geophys. Res. Atmos., 104(D24), 31333–31349, doi:10.1029/1999JD900923, 1999.
- 445 Eck, T. F., Holben, B. N., Ward, D. E., Mukelabai, M. M., Dubovik, O., Smirnov, A., Schafer, J. S., Hsu,  
 446 N. C., Piketh, S. J., Queface, A., Roux, J. Le, Swap, R. J. and Slutsker, I.: Variability of biomass burning  
 447 aerosol optical characteristics in southern Africa during the SAFARI 2000 dry season campaign and a  
 448 comparison of single scattering albedo estimates from radiometric measurements, J. Geophys. Res.  
 449 Atmos., 108(D13), doi:https://doi.org/10.1029/2002JD002321, 2003.
- 450 Fauchereau, N., Pohl, B., Reason, C. J. C., Rouault, M. and Richard, Y.: Recurrent daily OLR patterns in  
 451 the Southern Africa/Southwest Indian Ocean region, implications for South African rainfall and  
 452 teleconnections, Clim. Dyn., 32(4), 575–591, doi:10.1007/s00382-008-0426-2, 2009.
- 453 Flemming, J., Benedetti, A., Inness, A., Engelen, R. J., Jones, L., Huijnen, V., Remy, S., Parrington, M.,  
 454 Suttie, M., Bozzo, A., Peuch, V.-H., Akritidis, D. and Katragkou, E.: The CAMS interim Reanalysis of  
 455 Carbon Monoxide, Ozone and Aerosol for 2003–2015, Atmos. Chem. Phys., 17(3), 1945–1983,  
 456 doi:10.5194/acp-17-1945-2017, 2017.
- 457 Formenti, P., Elbert, W., Maenhaut, W., Haywood, J., Osborne, S. and Andreae, M. O.: Inorganic and  
 458 carbonaceous aerosols during the Southern African Regional Science Initiative (SAFARI 2000)  
 459 experiment: Chemical characteristics, physical properties, and emission data for smoke from African  
 460 biomass burning, J. Geophys. Res. Atmos., 108(D13), doi:https://doi.org/10.1029/2002JD002408,  
 461 2003.
- 462 Formenti, P., D'Anna, B., Flamant, C., Mallet, M., Piketh, S. J., Schepanski, K., Waquet, F., Auriol, F.,  
 463 Brogniez, G., Burnet, F., Chaboureaud, J.-P., Chauvigné, A., Chazette, P., Denjean, C., Desboeufs, K.,  
 464 Doussin, J.-F., Elguindi, N., Feuerstein, S., Gaetani, M., Giorio, C., Klopfer, D., Mallet, M. D., Nabat, P.,  
 465 Monod, A., Solmon, F., Namwoonde, A., Chikwililwa, C., Mushi, R., Welton, E. J. and Holben, B.: The  
 466 Aerosols, Radiation and Clouds in Southern Africa Field Campaign in Namibia: Overview, Illustrative  
 467 Observations, and Way Forward, Bull. Am. Meteorol. Soc., 100(7), 1277–1298, doi:10.1175/BAMS-D-  
 468 17-0278.1, 2019.





- 469 Gao, X., Sorooshian, S., Li, J. and Xu, J.: SST data improve modeling of North American monsoon  
 470 rainfall, *Eos, Trans. Am. Geophys. Union*, 84(43), 457, doi:10.1029/2003EO430001, 2003.
- 471 Gao, Y., Yu, S., Sherrell, R. M., Fan, S., Bu, K. and Anderson, J. R.: Particle-Size Distributions and  
 472 Solubility of Aerosol Iron Over the Antarctic Peninsula During Austral Summer, *J. Geophys. Res.*  
 473 *Atmos.*, 125(11), e2019JD032082, doi:https://doi.org/10.1029/2019JD032082, 2020.
- 474 Garstang, M., Tyson, P. D., Swap, R., Edwards, M., Kållberg, P. and Lindesay, J. A.: Horizontal and  
 475 vertical transport of air over southern Africa, *J. Geophys. Res. Atmos.*, 101(D19), 23721–23736,  
 476 doi:https://doi.org/10.1029/95JD00844, 1996.
- 477 Giles, D. M., Sinyuk, A., Sorokin, M. S., Schafer, J. S., Smirnov, A., Slutsker, I., Eck, T. F., Holben, B. N.,  
 478 Lewis, J., Campbell, J., Welton, E. J., Korkin, S. and Lyapustin, A.: Advancements in the Aerosol  
 479 Robotic Network (AERONET) Version 3 Database & Automated Near Real-Time Quality  
 480 Control Algorithm with Improved Cloud Screening for Sun Photometer Aerosol Optical Depth (AOD)  
 481 Measurements, *Atmos. Meas. Tech. Discuss.*, 1–78, doi:10.5194/amt-2018-272, 2018.
- 482 Haywood, J. M., Osborne, S. R., Francis, P. N., Keil, A., Formenti, P., Andreae, M. O. and Kaye, P. H.:  
 483 The mean physical and optical properties of regional haze dominated by biomass burning aerosol  
 484 measured from the C-130 aircraft during SAFARI 2000, *J. Geophys. Res. Atmos.*, 108(D13), n/a-n/a,  
 485 doi:10.1029/2002JD002226, 2003.
- 486 Haywood, J. M., Abel, S. J., Barrett, P. A., Bellouin, N., Blyth, A., Bower, K. N., Brooks, M., Carslaw, K.,  
 487 Che, H., Coe, H., Cotterell, M. I., Crawford, I., Cui, Z., Davies, N., Dingley, B., Field, P., Formenti, P.,  
 488 Gordon, H., de Graaf, M., Herbert, R., Johnson, B., Jones, A. C., Langridge, J. M., Malavelle, F.,  
 489 Partridge, D. G., Peers, F., Redemann, J., Stier, P., Szpek, K., Taylor, J. W., Watson-Parris, D., Wood,  
 490 R., Wu, H. and Zuidema, P.: The CLOUD–Aerosol–Radiation Interaction and Forcing: Year 2017  
 491 (CLARIFY-2017) measurement campaign, *Atmos. Chem. Phys.*, 21(2), 1049–1084, doi:10.5194/acp-  
 492 21-1049-2021, 2021.
- 493 Horowitz, H. M., Garland, R. M., Thatcher, M., Landman, W. A., Dedekind, Z., van der Merwe, J. and  
 494 Engelbrecht, F. A.: Evaluation of climate model aerosol seasonal and spatial variability over Africa  
 495 using AERONET, *Atmos. Chem. Phys.*, 17(22), 13999–14023, doi:10.5194/acp-17-13999-2017, 2017.
- 496 Hoskins, B. J. and Ambrizzi, T.: Rossby Wave Propagation on a Realistic Longitudinally Varying Flow, *J.*  
 497 *Atmos. Sci.*, 50(12), 1661–1671, doi:10.1175/1520-0469(1993)050<1661:RWPOAR>2.0.CO;2, 1993.
- 498 Hu, S. and Fedorov, A. V.: The extreme El Niño of 2015–2016 and the end of global warming hiatus,  
 499 *Geophys. Res. Lett.*, 44(8), 3816–3824, doi:10.1002/2017GL072908, 2017.
- 500 Huang, B., Thorne, P. W., Banzon, V. F., Boyer, T., Chepurin, G., Lawrimore, J. H., Menne, M. J., Smith,



- 501 T. M., Vose, R. S. and Zhang, H.-M.: Extended Reconstructed Sea Surface Temperature, Version 5
- 502 (ERSSTv5): Upgrades, Validations, and Intercomparisons, *J. Clim.*, 30(20), 8179–8205,
- 503 doi:10.1175/JCLI-D-16-0836.1, 2017.
- 504 Limpasuvan, V. and Hartmann, D. L.: Eddies and the annular modes of climate variability, *Geophys.*
- 505 *Res. Lett.*, 26(20), 3133–3136, doi:10.1029/1999GL010478, 1999.
- 506 Lindsay, J. A., Andreae, M. O., Goldammer, J. G., Harris, G., Annegarn, H. J., Garstang, M., Scholes,
- 507 R. J. and van Wilgen, B. W.: International geosphere-biosphere programme/international global
- 508 atmospheric chemistry SAFARI-92 field experiment: Background and overview, *J. Geophys. Res.*
- 509 *Atmos.*, 101(D19), 23521–23530, doi:https://doi.org/10.1029/96JD01512, 1996.
- 510 Macron, C., Pohl, B., Richard, Y. and Bessafi, M.: How do tropical temperate troughs form and
- 511 develop over Southern Africa?, *J. Clim.*, 27(4), 1633–1647, doi:10.1175/JCLI-D-13-00175.1, 2014.
- 512 Mallet, M., Solmon, F., Nabat, P., Elguindi, N., Waquet, F., Bouniol, D., Sayer, A. M., Meyer, K.,
- 513 Roehrig, R., Michou, M., Zuidema, P., Flamant, C., Redemann, J. and Formenti, P.: Direct and semi-
- 514 direct radiative forcing of biomass-burning aerosols over the southeast Atlantic (SEA) and its
- 515 sensitivity to absorbing properties: a regional climate modeling study, *Atmos. Chem. Phys.*, 20(21),
- 516 13191–13216, doi:10.5194/acp-20-13191-2020, 2020.
- 517 McMillan, W. W., McCourt, M. L., Revercomb, H. E., Knuteson, R. O., Christian, T. J., Doddridge, B. G.,
- 518 Hobbs, P. V., Lukovich, J. V., Novelli, P. C., Piketh, S. J., Sparling, L., Stein, D., Swap, R. J. and Yokelson,
- 519 R. J.: Tropospheric carbon monoxide measurements from the Scanning High-Resolution
- 520 Interferometer Sounder on 7 September 2000 in southern Africa during SAFARI 2000, *J. Geophys.*
- 521 *Res. Atmos.*, 108(D13), n/a-n/a, doi:10.1029/2002JD002335, 2003.
- 522 Michelangeli, P. A., Vautard, R. and Legras, B.: Weather regimes: recurrence and quasi stationarity, *J.*
- 523 *Atmos. Sci.*, 52(8), 1237–1256, doi:10.1175/1520-0469(1995)052<1237:WRRAS>2.0.CO;2, 1995.
- 524 Pistone, K., Redemann, J., Doherty, S., Zuidema, P., Burton, S., Cairns, B., Cochrane, S., Ferrare, R.,
- 525 Flynn, C., Freitag, S., Howell, S. G., Kacenelenbogen, M., LeBlanc, S., Liu, X., Schmidt, K. S., Sedlacek
- 526 III, A. J., Segal-Rozenhaimer, M., Shinozuka, Y., Stamnes, S., van Diedenhoven, B., Van Harten, G. and
- 527 Xu, F.: Intercomparison of biomass burning aerosol optical properties from in situ and remote-
- 528 sensing instruments in ORACLES-2016, *Atmos. Chem. Phys.*, 19(14), 9181–9208, doi:10.5194/acp-19-
- 529 9181-2019, 2019.
- 530 Pohl, B. and Fauchereau, N.: The southern annular mode seen through weather regimes, *J. Clim.*,
- 531 25(9), 3336–3354, doi:10.1175/JCLI-D-11-00160.1, 2012.
- 532 Pohl, B., Dieppois, B., Crétat, J., Lawler, D. and Rouault, M.: From synoptic to interdecadal variability



- 533 in southern African rainfall: Toward a unified view across time scales, *J. Clim.*, 31(15), 5845–5872,  
 534 doi:10.1175/JCLI-D-17-0405.1, 2018.
- 535 Rayner, N. A., Parker, D. E., Horton, E. B., Folland, C. K., Alexander, L. V., Rowell, D. P., Kent, E. C. and  
 536 Kaplan, A.: Global analyses of sea surface temperature, sea ice, and night marine air temperature  
 537 since the late nineteenth century, *J. Geophys. Res. Atmos.*, 108(14), doi:10.1029/2002jd002670,  
 538 2003.
- 539 Redemann, J., Wood, R., Zuidema, P., Doherty, S. J., Luna, B., LeBlanc, S. E., Diamond, M. S.,  
 540 Shinozuka, Y., Chang, I. Y., Ueyama, R., Pfister, L., Ryoo, J.-M., Dobracki, A. N., da Silva, A. M., Longo,  
 541 K. M., Kacenelenbogen, M. S., Flynn, C. J., Pistone, K., Knox, N. M., Piketh, S. J., Haywood, J. M.,  
 542 Formenti, P., Mallet, M., Stier, P., Ackerman, A. S., Bauer, S. E., Fridlind, A. M., Carmichael, G. R.,  
 543 Saide, P. E., Ferrada, G. A., Howell, S. G., Freitag, S., Cairns, B., Holben, B. N., Knobelspiesse, K. D.,  
 544 Tanelli, S., L'Ecuyer, T. S., Dzambo, A. M., Sy, O. O., McFarquhar, G. M., Poellot, M. R., Gupta, S.,  
 545 O'Brien, J. R., Nenes, A., Kacarab, M., Wong, J. P. S., Small-Griswold, J. D., Thornhill, K. L., Noone, D.,  
 546 Podolske, J. R., Schmidt, K. S., Pilewskie, P., Chen, H., Cochrane, S. P., Sedlacek, A. J., Lang, T. J., Stith,  
 547 E., Segal-Rozenhaimer, M., Ferrare, R. A., Burton, S. P., Hostetler, C. A., Diner, D. J., Seidel, F. C.,  
 548 Platnick, S. E., Myers, J. S., Meyer, K. G., Spangenberg, D. A., Maring, H. and Gao, L.: An overview of  
 549 the ORACLES (ObseRvations of Aerosols above CLouds and their intEractionS) project: aerosol–  
 550 cloud–radiation interactions in the southeast Atlantic basin, *Atmos. Chem. Phys.*, 21(3), 1507–1563,  
 551 doi:10.5194/acp-21-1507-2021, 2021.
- 552 Stier, P., Schutgens, N. A. J., Bellouin, N., Bian, H., Boucher, O., Chin, M., Ghan, S., Huneeus, N.,  
 553 Kinne, S., Lin, G., Ma, X., Myhre, G., Penner, J. E., Randles, C. A., Samset, B., Schulz, M., Takemura, T.,  
 554 Yu, F., Yu, H. and Zhou, C.: Host model uncertainties in aerosol radiative forcing estimates: Results  
 555 from the AeroCom Prescribed intercomparison study, *Atmos. Chem. Phys.*, 13(6), 3245–3270,  
 556 doi:10.5194/acp-13-3245-2013, 2013.
- 557 von Storch, H. and Zwiers, F. W.: *Statistical Analysis in Climate Research*, Cambridge University Press,  
 558 Cambridge, 1999.
- 559 Swap, R., Garstang, M., Macko, S. A., Tyson, P. D., Maenhaut, W., Artaxo, P., Kållberg, P. and Talbot,  
 560 R.: The long-range transport of southern African aerosols to the tropical South Atlantic, *J. Geophys.*  
 561 *Res. Atmos.*, 101(D19), 23777–23791, doi:10.1029/95JD01049, 1996.
- 562 Swap, R. J., Annegarn, H. J., Suttles, J. T., King, M. D., Platnick, S., Privette, J. L. and Scholes, R. J.:  
 563 Africa burning: A thematic analysis of the Southern African Regional Science Initiative (SAFARI 2000),  
 564 *J. Geophys. Res. Atmos.*, 108(D13), n/a-n/a, doi:10.1029/2003JD003747, 2003.



- 565 Tang, C., Morel, B., Wild, M., Pohl, B., Abiodun, B. and Bessafi, M.: Numerical simulation of surface  
 566 solar radiation over Southern Africa. Part 1: Evaluation of regional and global climate models, *Clim.*  
 567 *Dyn.*, 52(1–2), 457–477, doi:10.1007/s00382-018-4143-1, 2019.
- 568 Tyson, P. D.: Atmospheric transport of aerosols and trace gases over southern Africa, *Prog. Phys.*  
 569 *Geogr. Earth Environ.*, 21(1), 79–101, doi:10.1177/030913339702100105, 1997.
- 570 Vigaud, N., Pohl, B. and Crétat, J.: Tropical-temperate interactions over southern Africa simulated by  
 571 a regional climate model, *Clim. Dyn.*, 39(12), 2895–2916, doi:10.1007/s00382-012-1314-3, 2012.
- 572 Wai, K. M., Wu, S., Kumar, A. and Liao, H.: Seasonal variability and long-term evolution of  
 573 tropospheric composition in the tropics and Southern Hemisphere, *Atmos. Chem. Phys.*, 14(10),  
 574 4859–4874, doi:10.5194/acp-14-4859-2014, 2014.
- 575 van der Werf, G. R., Randerson, J. T., Giglio, L., Collatz, G. J., Mu, M., Kasibhatla, P. S., Morton, D. C.,  
 576 DeFries, R. S., Jin, Y. and van Leeuwen, T. T.: Global fire emissions and the contribution of  
 577 deforestation, savanna, forest, agricultural, and peat fires (1997–2009), *Atmos. Chem. Phys.*, 10(23),  
 578 11707–11735, doi:10.5194/acp-10-11707-2010, 2010.
- 579 van der Werf, G. R., Randerson, J. T., Giglio, L., van Leeuwen, T. T., Chen, Y., Rogers, B. M., Mu, M.,  
 580 van Marle, M. J. E., Morton, D. C., Collatz, G. J., Yokelson, R. J. and Kasibhatla, P. S.: Global fire  
 581 emissions estimates during 1997–2016, *Earth Syst. Sci. Data*, 9(2), 697–720, doi:10.5194/essd-9-697-  
 582 2017, 2017.
- 583 Wu, H., Taylor, J. W., Szpek, K., Langridge, J. M., Williams, P. I., Flynn, M., Allan, J. D., Abel, S. J., Pitt,  
 584 J., Cotterell, M. I., Fox, C., Davies, N. W., Haywood, J. and Coe, H.: Vertical variability of the  
 585 properties of highly aged biomass burning aerosol transported over the southeast Atlantic during  
 586 CLARIFY-2017, *Atmos. Chem. Phys.*, 20(21), 12697–12719, doi:10.5194/acp-20-12697-2020, 2020.
- 587 Zuidema, P., Chang, P., Medeiros, B., Kirtman, B. P., Mechoso, R., Schneider, E. K., Toniazzo, T.,  
 588 Richter, I., Small, R. J., Bellomo, K., Brandt, P., De Szoeko, S., Farrar, J. T., Jung, E., Kato, S., Li, M.,  
 589 Patricola, C., Wang, Z., Wood, R. and Xu, Z.: Challenges and prospects for reducing coupled climate  
 590 model sst biases in the eastern tropical atlantic and pacific oceans: The U.S. Clivar eastern tropical  
 591 oceans synthesis working group, *Bull. Am. Meteorol. Soc.*, 97(12), 2305–2327, doi:10.1175/BAMS-D-  
 592 15-00274.1, 2016.



**Table 1.** AERONET station used in this study: locations and data availability (Version 3 Direct Sun algorithm, level2).

Station	Country	Latitude	Longitude	Observations (coverage)
Ascension Island (AI)	UK Overseas Territory	8.0°S	14.4°W	612 (2003-2017)
Bonanza (BO)	Namibia	21.8°S	19.6°E	126 (2016-2017)
Gobabeb (GO)	Namibia	23.6°S	15.0°E	219 (2015-2017)
Henties Bay (HB)	Namibia	22.1°S	14.3°E	139 (2013-2017)
HESS (HE)	Namibia	23.3°S	16.5°E	158 (2016-2017)
Simon's Town IMT (ST)	South Africa	34.2°S	18.4°E	127 (2016-2017)
Upington (UP)	South Africa	28.4°S	21.2°E	111 (2015-2016)

**Table 2.** WR transition rate, computed as the fraction of transition from a WR (rows) into the others (columns). By definition, the diagonal represents persistence. Transition rates above 1/6 are reported in bold.

WR	1	2	3	4	5	6
1	<b>0.39</b>	0.08	0.08	0.03	<b>0.28</b>	0.14
2	0.06	<b>0.61</b>	0.06	0.08	0.11	0.06
3	0.04	0.12	<b>0.45</b>	<b>0.24</b>	0.06	0.09
4	<b>0.29</b>	0.12	0.03	<b>0.40</b>	0.03	0.13
5	0.03	0.12	<b>0.31</b>	0.02	<b>0.46</b>	0.05
6	0.05	0.10	0.08	0.07	0.10	<b>0.59</b>

**Table 3.** Circulation-to-environment characterisation: P-values of ANOVA and Kolmogorov-Smirnov test on AOD anomalies at the AERONET stations (Table 1). Values lower than 0.05 are reported in bold.

Station	ANOVA	WR1	WR2	WR3	WR4	WR5	WR6
Ascension Island (AI)	<b>0.01</b>	0.91	0.23	0.08	0.27	0.89	<b>0.04</b>
Bonanza (BO)	0.07	0.31	0.67	0.90	<b>0.01</b>	0.76	0.35
Gobabeb (GO)	<b>&lt;0.01</b>	<b>0.01</b>	0.90	0.55	0.07	0.98	<b>&lt;0.01</b>
Henties Bay (HB)	<b>&lt;0.01</b>	<b>&lt;0.01</b>	0.77	0.70	0.13	0.49	0.18
HESS (HE)	<b>&lt;0.01</b>	<b>&lt;0.01</b>	0.26	<b>&lt;0.01</b>	0.93	0.71	0.36
Simon's Town IMT (ST)	0.09	0.26	0.27	0.91	0.87	0.13	0.61
Upington (UP)	<b>&lt;0.01</b>	<b>0.03</b>	0.87	<b>&lt;0.01</b>	<b>0.02</b>	0.64	0.23

**Table 4.** Environment-to-circulation characterisation: Chi-squared statistics for each quartile (Q1-4) at the AERONET stations (Table 1). Values exceeding 11.07, i.e. the critical threshold for the Chi-squared distribution with 5 degrees of freedom at 95% level of confidence, are reported in bold.

Station	Q1	Q2	Q3	Q4
Ascension Island (AI)	8.05	2.99	<b>11.19</b>	9.31
Bonanza (BO)	3.91	2.82	1.28	7.35
Gobabeb (GO)	<b>12.29</b>	1.99	10.68	<b>17.03</b>
Henties Bay (HB)	6.45	6.98	6.16	<b>11.49</b>
HESS (HE)	<b>15.04</b>	7.99	<b>12.59</b>	<b>12.16</b>
Simon's Town IMT (ST)	5.93	1.79	11.04	<b>17.30</b>
Upington (UP)	<b>14.29</b>	10.14	3.86	<b>25.23</b>

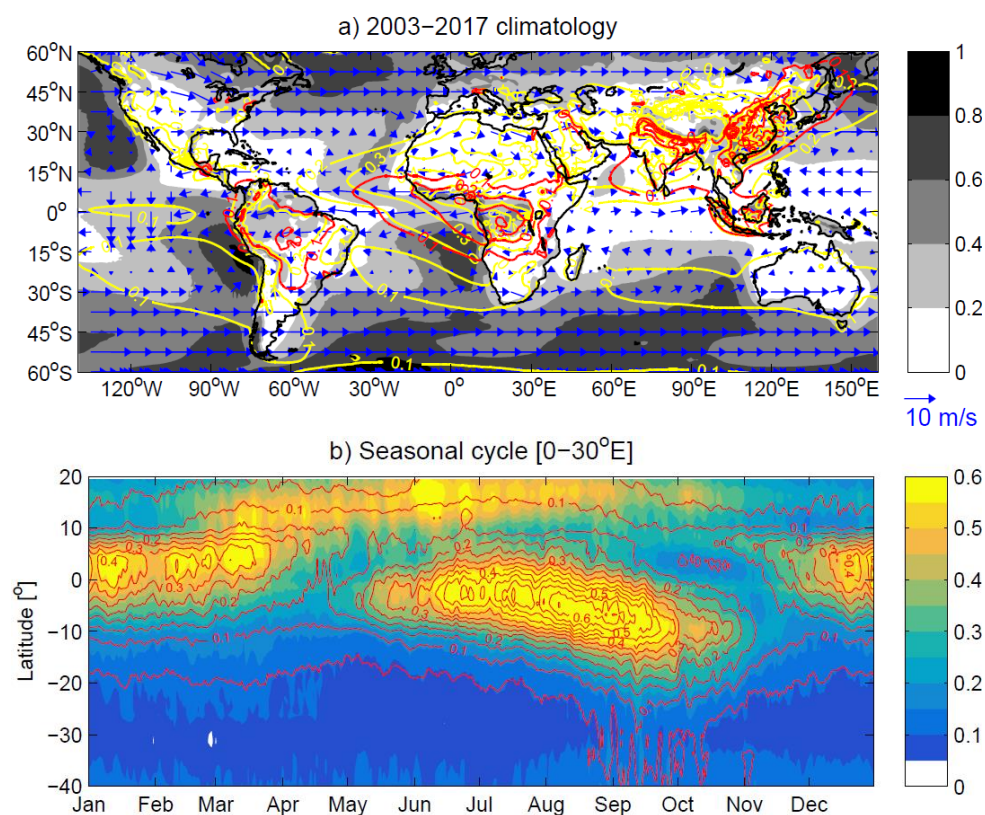


**Figure 1.** 2003–2017 climatology derived from CAMS reanalysis: (a) annual mean of total (yellow contours) and organic matter (red contours) AOD at 550 nm, low cloud cover fraction (shadings) and wind at 700 hPa (arrows); (b) annual cycle of total (shadings) and organic matter (red contours) AOD at 550 nm, averaged over [0–30°E].

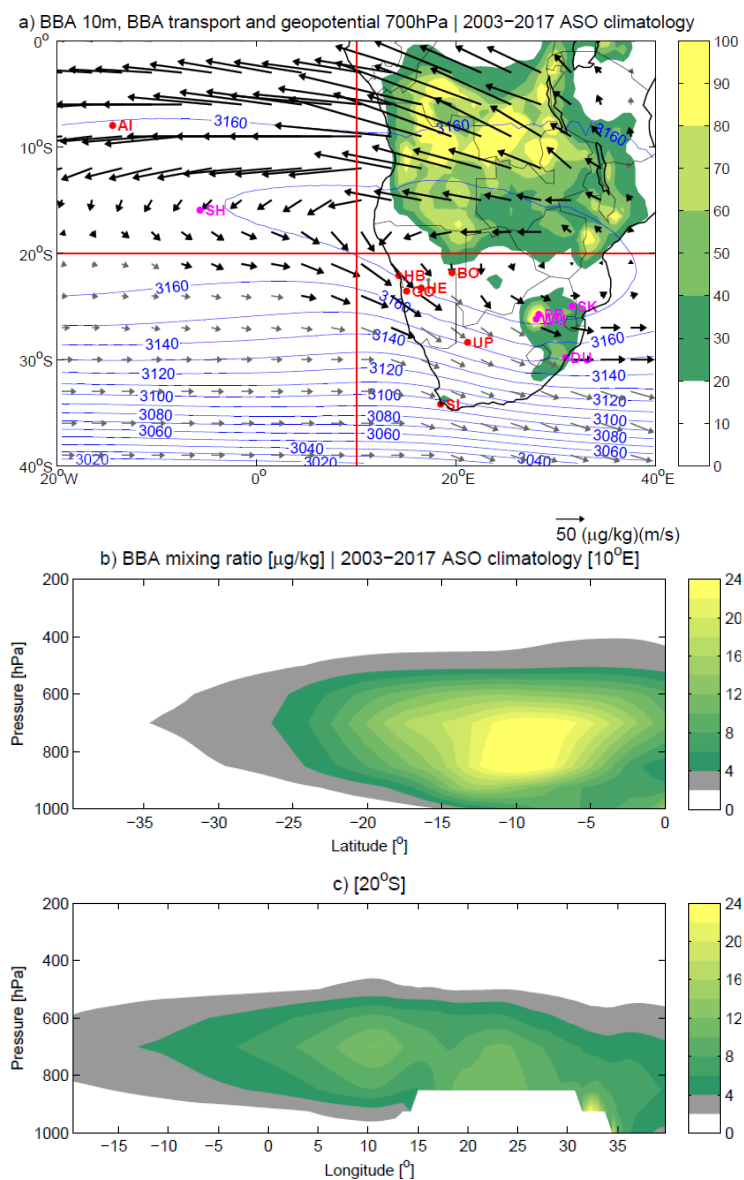


**Figure 2.** 2003-2017 ASO climatology derived from CAMS reanalysis: (a) BBA mixing ratio at 10m ( $\mu\text{g/kg}$ , shadings), BBA transport at 700 hPa ( $\mu\text{g/kg m/s}$ , arrows) and geopotential height at 700 hPa (m, contours); thick arrows highlight BBA transport corresponding to BBA mixing ratio greater than 4  $\mu\text{g/kg}$ . Red lines indicate where BBA mixing ratio cross-sections are computed, red dots indicate the locations of the AERONET stations used in this study (see Table 1 for details), magenta dots indicate the locations of available stations not used in this study (see Section 2 for details). Vertical cross-sections of the BBA mixing ratio ( $\mu\text{g/kg}$ ) at (b) 0°E and (c) 25°S.



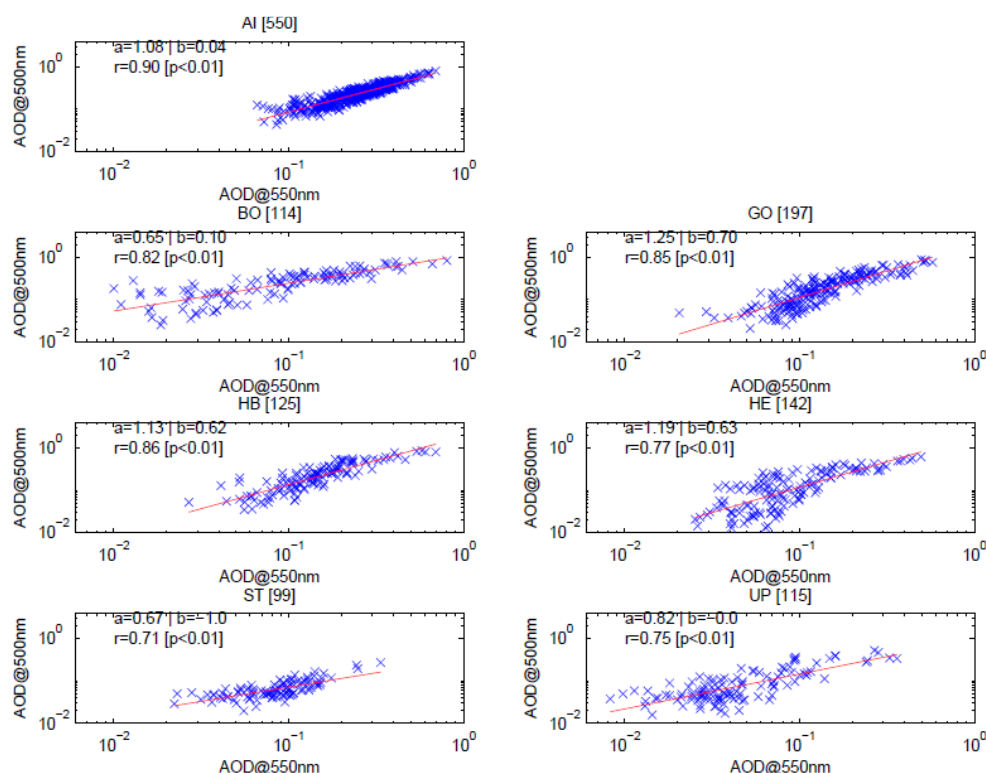


**Figure 3.** CAMS vs AERONET daily data comparison for ASO 2003-2017: CAMS reanalysis AOD at 500 nm vs AERONET observed AOD at 500 nm. CAMS data are extracted at grid points the closest to the station coordinates (Table 1). Red lines display the linear regression between CAMS and AERONET data, and the coefficients of the regression models are also reported in the plots, along with the correlation coefficient and the p-value. In titles, the size of the sample used in the linear regression model is reported in brackets (see Section 2 for details).



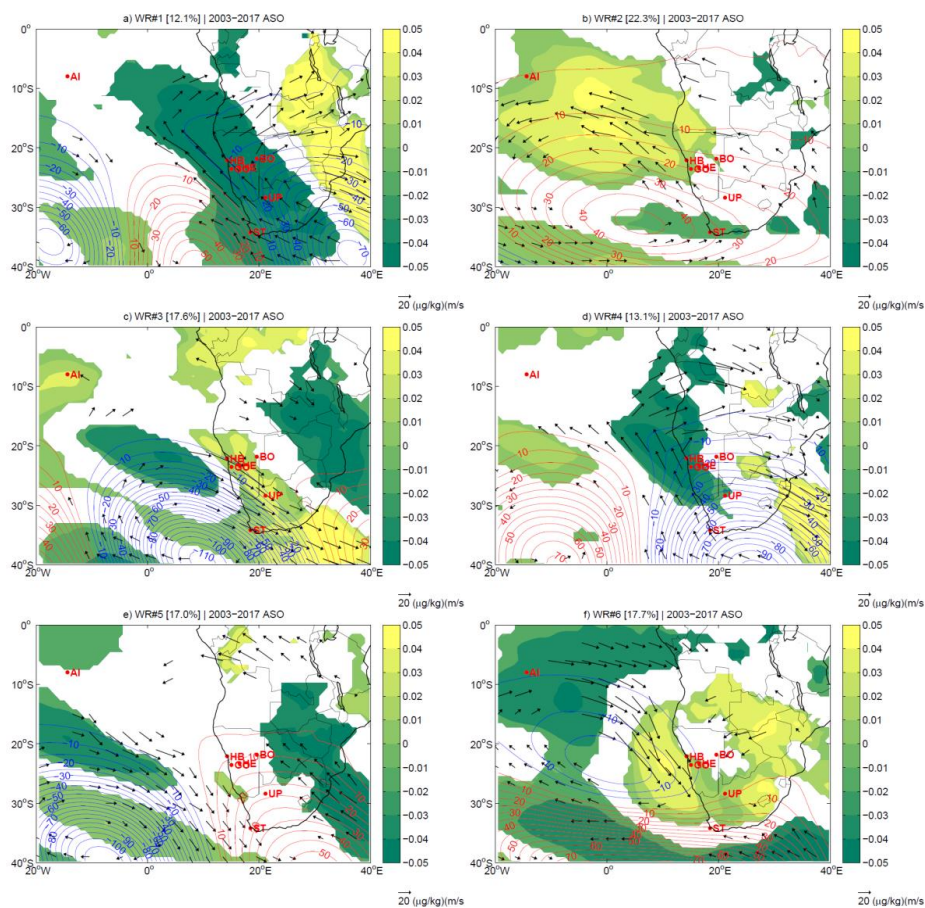


**Figure 4.** Anomaly patterns of CAMS geopotential height (m, contours), AOD at 550 nm (shadings) and BBA transport ( $(\mu\text{g/kg})(\text{m/s})$ , arrows) at 700 hPa associated with the WRs classified from the geopotential height at 700 hPa in ASO 2003-2017. Frequency of the WRs is indicated in brackets; for AOD and BBA transport, only values significant at 95% level of confidence for a Student's t-test are displayed.

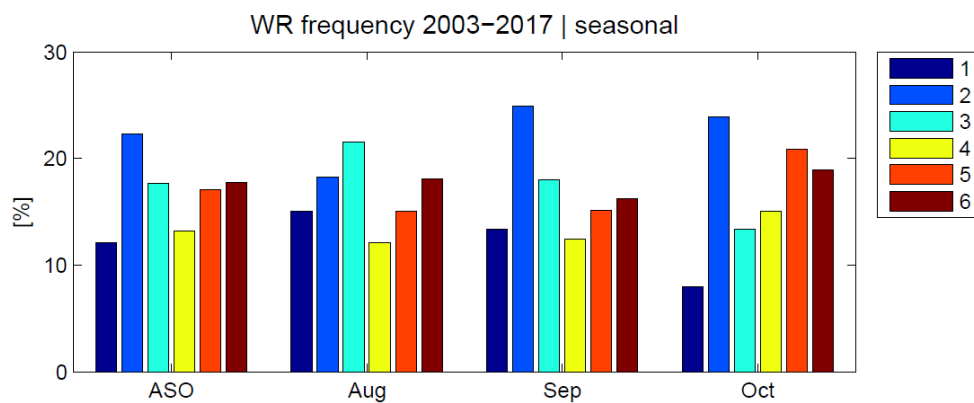


**Figure 5.** WR frequency 2003–2017: seasonal and monthly.

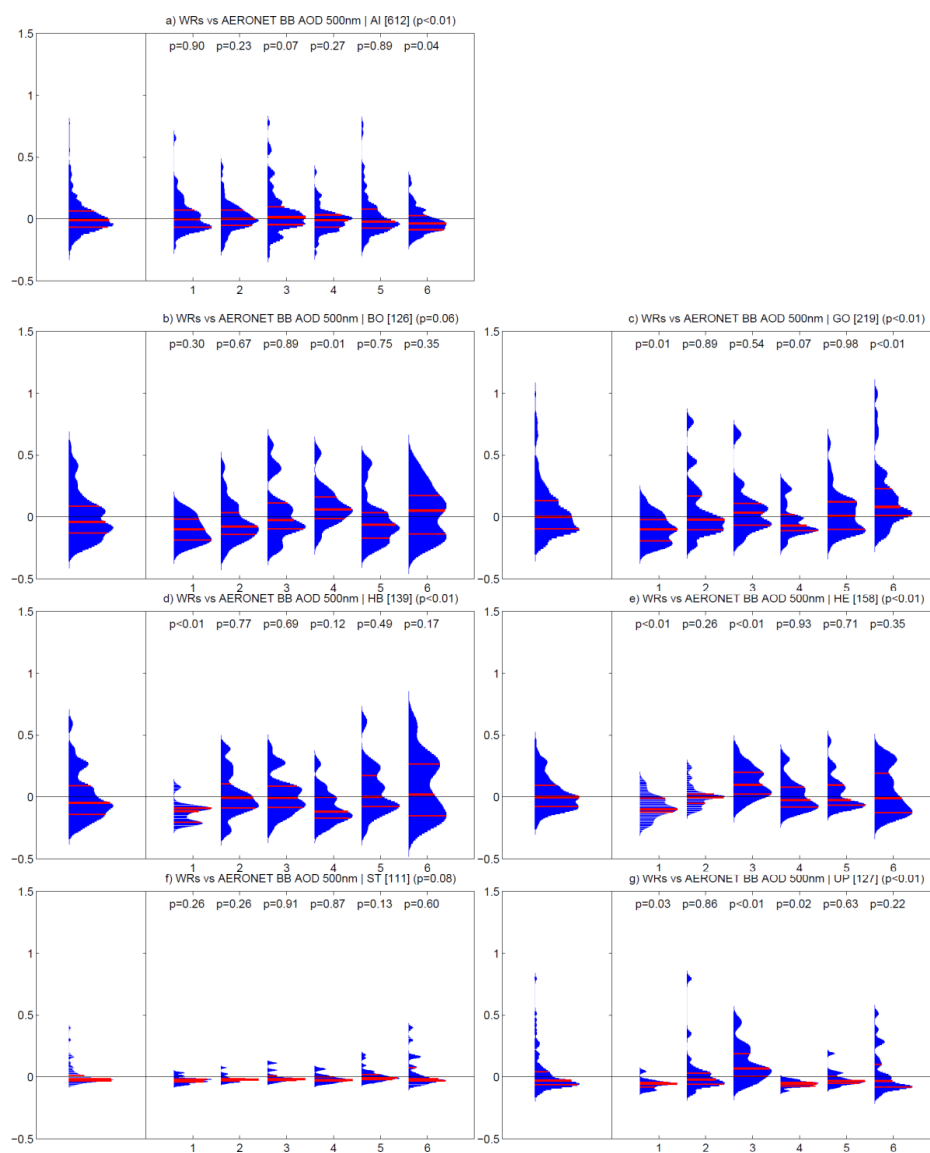


**Figure 6.** Circulation to environment characterisation: distributions of the AOD anomalies at 500 nm at the AERONET stations (Table 1), and as a function of the WRs. Probability density functions are estimated by using a normal kernel density; red lines represent 25th, 50th and 75th percentiles. For each WR, the p-value of a Kolmogorov-Smirnov test used to assess the difference with the total sample is reported. In titles, in brackets the number of available daily observations and the p-value of the ANOVA used to assess the WR characterisation are reported.

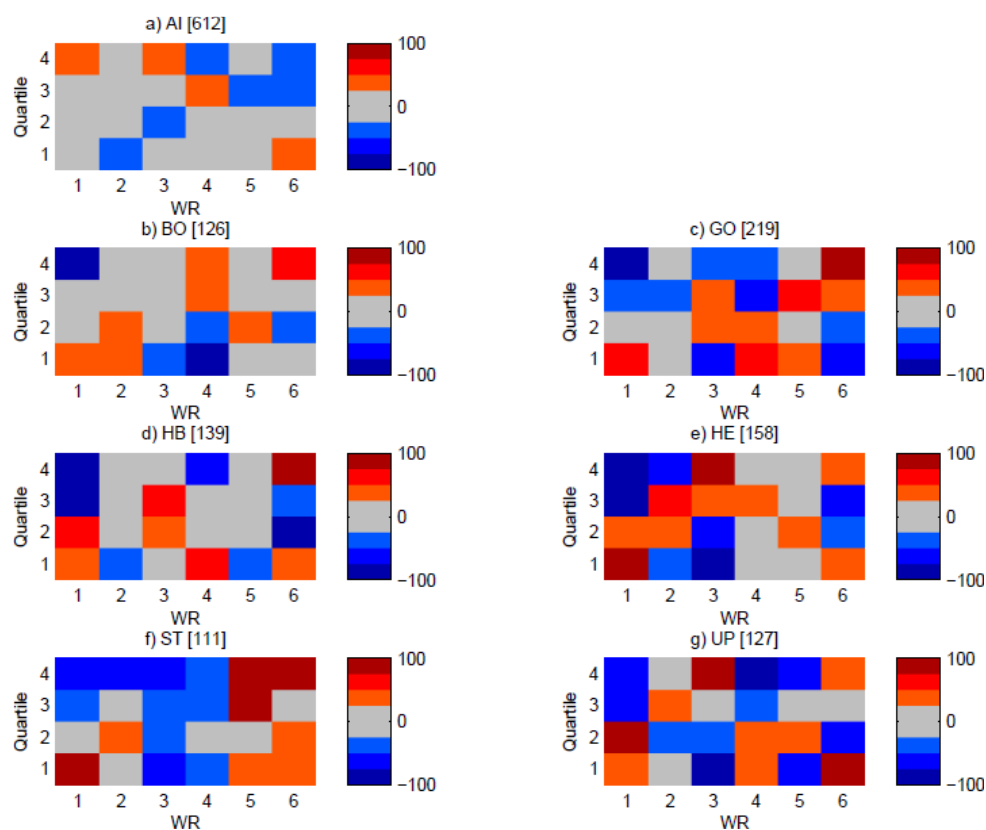


**Figure 7.** Environment to circulation characterisation: WR frequency anomaly as a function of the quartiles of the AOD anomalies at 500 nm at the AERONET stations (Table 1). Values are percentage changes relative to climatological frequencies. In brackets, the number of available daily observations are indicated.

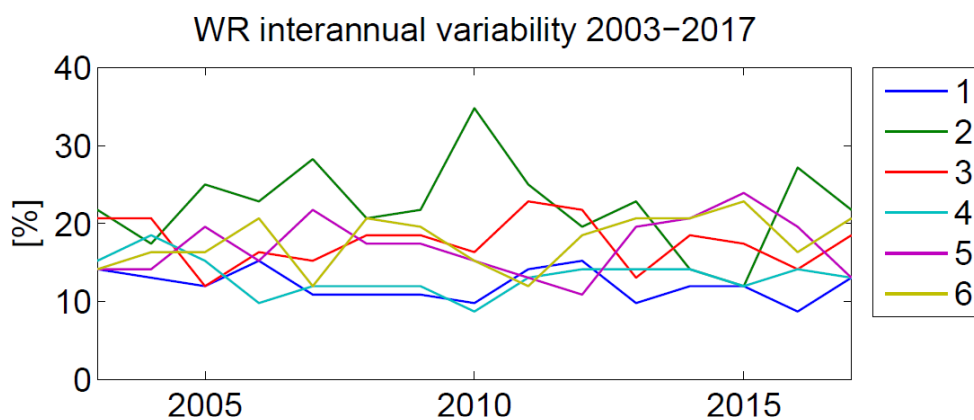


**Figure 8.** WR frequency 2003–2017: interannual variability.

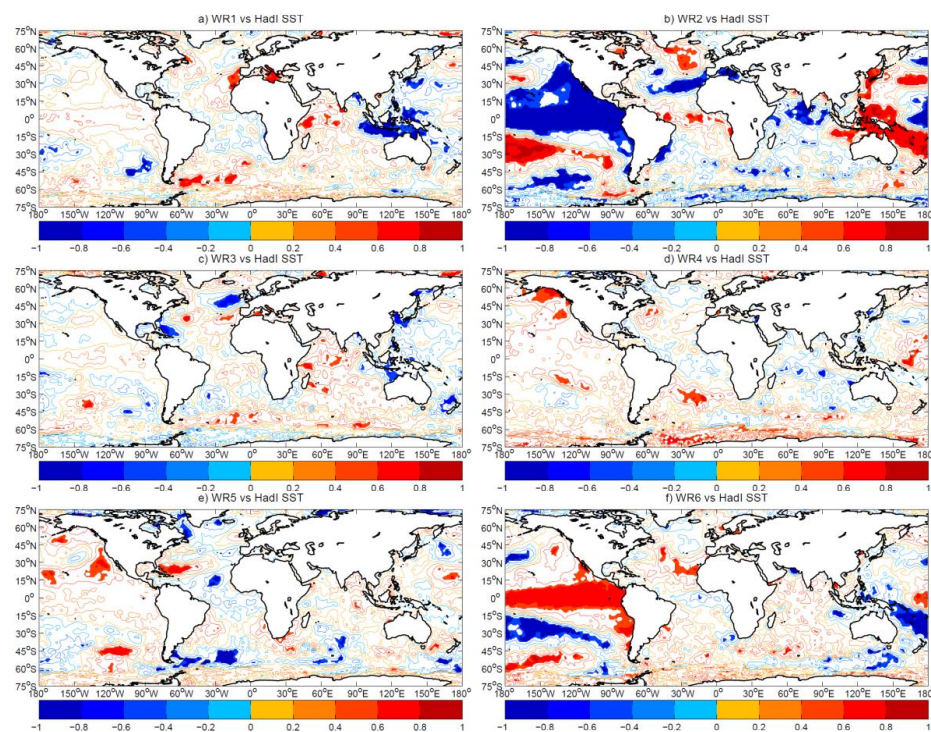


**Figure 9.** Interannual correlation over the period 2003-2017: WR frequency vs Hadl SST in ASO. Shadings display significant correlations at 95% level of confidence. Time series are detrended and standardised.

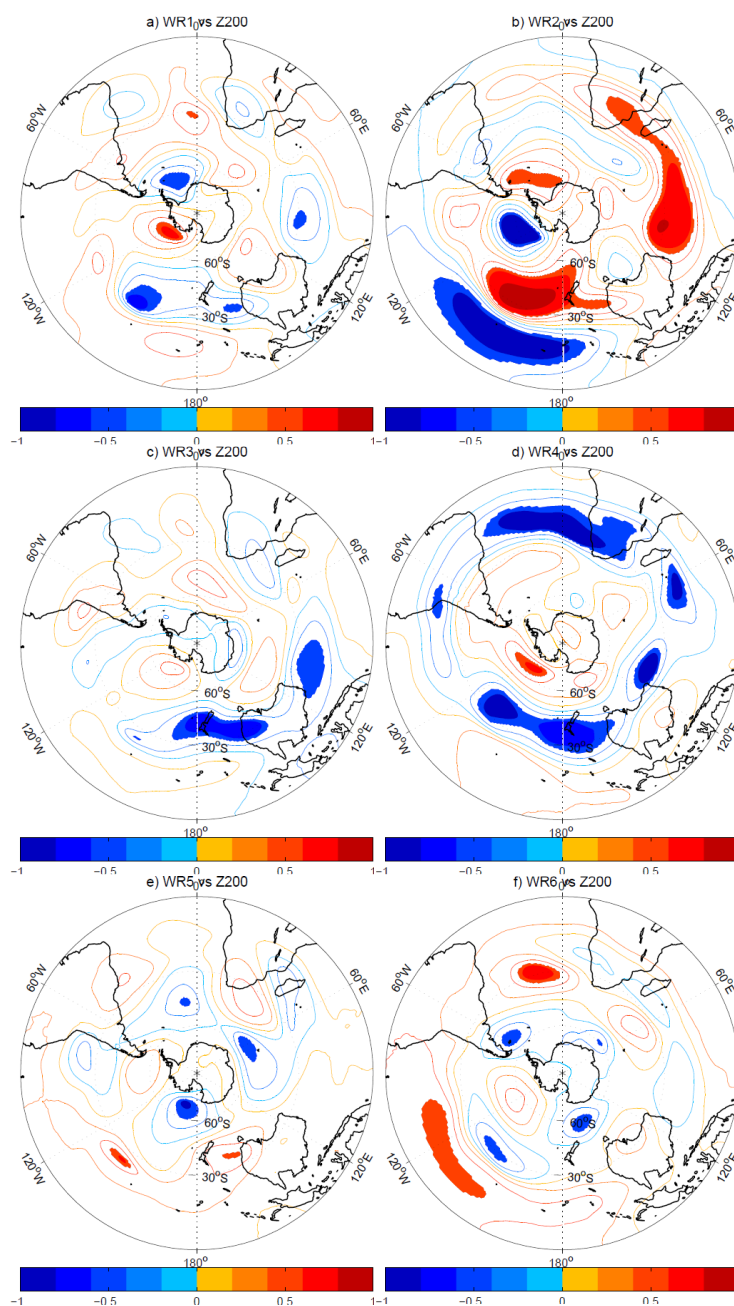


**Figure 10.** Interannual correlation over the period 2003-2017: WR frequency vs geopotential height at 200 hPa in ASO. Shadings display significant correlations at 95% level of confidence. Time series are detrended and standardised.



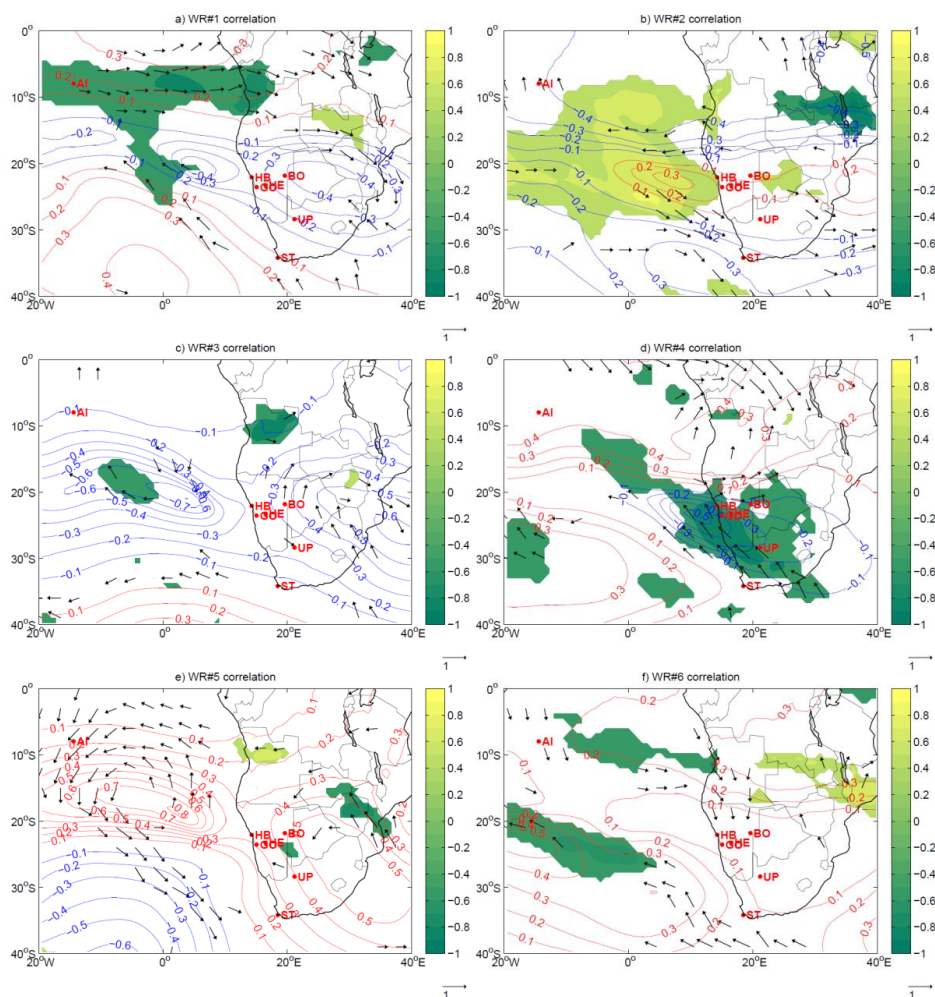


**Figure 11.** Correlation maps of WR frequency vs CAMS geopotential height (contours), AOD at 550 nm (shadings) and BBA transport (arrows) at 700 hPa. For AOD and BBA transport, only correlation significant at 95% level of confidence are displayed. Time series are detrended and standardised.